

# Topological superconductivity in two-dimensional $\pi$ -junction Dirac semimetals

Yijie Mo,<sup>1</sup> Xiao-Jiao Wang,<sup>1</sup> and Zhongbo Yan<sup>1,\*</sup>

<sup>1</sup>*Guangdong Provincial Key Laboratory of Magnetoelectric Physics and Devices,  
State Key Laboratory of Optoelectronic Materials and Technologies,  
School of Physics, Sun Yat-sen University, Guangzhou 510275, China*

(Dated: March 11, 2025)

Odd-parity pairings offer a natural pathway for realizing topological superconductivity. When two identical even-parity superconductors form a  $\pi$ -junction, the metallic material sandwiched between them experiences an effective odd-parity pairing, facilitating the emergence of topological superconductivity in the intermediate region. In this work, we consider the intermediate material to be a two-dimensional spin-orbit-coupled Dirac semimetal. When the two superconductors are conventional  $s$ -wave superconductors, we find that a helical topological superconductor can be realized. This phase is characterized by the presence of a pair of helical Majorana edge states. Interestingly, when the superconductors are  $s_{\pm}$ -wave superconductors, we observe not only the helical topological superconductor but also an unconventional topological superconductor. The latter is distinguished by the existence of two pairs of helical Majorana edge states, despite the fact that the global topological invariants for this system take trivial values. By further applying an in-plane magnetic field, we demonstrate that second-order topological superconductors can be achieved. These phases host isolated Majorana corner modes as well as twofold Majorana corner modes. Our findings reveal that two-dimensional  $\pi$ -junction Dirac semimetals can support a rich variety of topological superconducting phases, offering a versatile platform for exploring exotic topological phenomena.

## I. INTRODUCTION

Topological superconductors (TSCs) have attracted considerable attention over the past two decades due to their intriguing properties [1–8] and promising applications in topological quantum computation [9–12]. Although superconductors featuring intrinsic odd-parity pairings are naturally predisposed to exhibit topological nontriviality [13–15], the scarcity of such intrinsic odd-parity superconductors in nature poses a significant challenge to realizing this potential [16]. Consequently, the search for alternative approaches to engineer effective odd-parity pairings has emerged as a central focus in the quest to realize TSCs. A key breakthrough in this pursuit has been the identification of spin-orbit coupling (SOC) as a pivotal mechanism for enabling effective odd-parity pairings [17]. Pioneering theoretical studies have demonstrated that the interplay of SOC, Zeeman (exchange) fields, and even-parity  $s$ -wave pairings can give rise to effective  $s$ -wave pairings [18–23]. This mechanism enables the realization of time-reversal-symmetry-breaking TSCs, including two-dimensional (2D) chiral TSCs hosting one-dimensional (1D) chiral Majorana edge modes [18–21], as well as 1D TSCs featuring zero-dimensional (0D) Majorana zero modes at their ends [22, 23]. These groundbreaking theoretical insights have driven remarkable progress in the experimental exploration of TSCs [24–30].

In recent years, the emergence of the concept of higher-order topology has sparked renewed interest in the study of TSCs [31–35], as it expands the classification of TSCs and enriches platforms for hosting Majorana modes [36–70], along with new mechanisms for their manipulation [38, 71–76]. With this expansion, TSCs are further categorized according to the codimension of the gapless Majorana modes

on their boundaries. Specially, an  $n$ th-order TSC is defined by the presence of gapless Majorana modes with a codimension  $d_c = n$  [35]. Within this classification scheme, conventional TSCs are regarded as first-order TSCs [77], as these gapless Majorana modes on their boundaries have a codimension of one. Interestingly, higher-order TSCs can be derived from first-order TSCs by selectively breaking their protecting symmetries. A notable example is the realization of a time-reversal-symmetry-breaking second-order TSC, achieved by applying an in-plane magnetic field to a helical TSC (a first-order TSC protected by time-reversal symmetry [78]) in two dimensions [34, 38]. This example highlights that symmetry-protected first-order TSCs are not only intrinsically interesting but can also serve as parent states for the generation of higher-order TSCs.

Despite being an intriguing topological phase, the experimental realization of 2D helical TSCs has remained elusive. To achieve this phase, two primary scenarios have been proposed. First, in the case of odd-parity pairing with an inversion-invariant Hamiltonian, the sole requirement for realization is the presence of an odd number of Kramers degenerate Fermi surfaces [79, 80]. In contrast, for even-parity pairing, inversion symmetry must be broken, and the Fermi surfaces must be spin-split by SOC. Additionally, the even-parity pairing must exhibit sign changes across the Brillouin zone, ensuring that among the even-numbered segments of the Fermi surface, an odd number of them have positive pairing signs, while the remaining odd number have negative pairing signs [81]. For the first scenario, existing theoretical proposals have primarily focused on interaction-driven intrinsic odd-parity pairing in doped thin-film or monolayer topological insulators (TIs) [82, 83], bilayer systems with inversion-symmetric SOC [84–86], as well as bilayer Fermi gas immersed in a Bose-Einstein condensate [87]. For the second scenario, representative theoretical proposals include heterostructures combining semiconductors with inversion-

\* [yanzhb5@mail.sysu.edu.cn](mailto:yanzhb5@mail.sysu.edu.cn)

asymmetric Rashba SOC and unconventional superconductors [88–90], as well as thin films of iron-based superconductors with Dirac surface states [91] or bulk Dirac points [92].

Interestingly, in addition to intrinsic interaction-driven odd-parity pairing, effective odd-parity pairing can also be induced through the superconducting proximity effect in a  $\pi$ -junction structure, as illustrated in Fig.1(a). Specifically, when two identical even-parity superconductors with a  $\pi$  phase difference are coupled, the intermediate material between them experiences an effective odd-parity pairing. Previous studies have demonstrated that this approach can realize 2D helical TSCs in a bilayer system with inversion-symmetric SOC when it is sandwiched between two conventional  $s$ -wave superconductors with a  $\pi$  phase difference [47], or in a thin film of TI when the pairings for the Dirac surface states at the top and bottom surfaces have a  $\pi$  phase difference [93, 94]. Inspired by these studies, we propose in this work to use a different class of topological materials as the intermediate layer: 2D spin-orbit-coupled Dirac semimetals (DSMs). These materials feature Dirac points in their band structure, which are stabilized by the combined action of time-reversal symmetry, inversion symmetry, and nonsymmorphic symmetries [95]. Furthermore, in addition to conventional  $s$ -wave superconductors, we also explore the use of unconventional superconductors with  $s_{\pm}$ -wave pairing, such as iron-based superconductors [96, 97], to construct the  $\pi$ -junction.

Our findings can be summarized as follows. When the  $\pi$ -junction is formed by two  $s$ -wave superconductors, we observe that a helical TSC characterized by the presence of a pair of helical Majorana edge states can be achieved. When the  $s$ -wave superconductors are replaced by  $s_{\pm}$ -wave superconductors, richer physics emerges. Specially, in addition to the helical TSC, we find that the system can host an unconventional first-order TSC phase when the pairing nodes lie between two Fermi surface segments. Interestingly, this phase is characterized by the presence of two pairs of helical Majorana edge states, suggesting that it is  $Z_2$  topologically trivial according to the tenfold-way classification [98–100]. The robustness of these two pairs of helical Majorana edge states can be attributed to weak topological invariants defined along high-symmetry lines within the Brillouin zone. By applying an in-plane magnetic field to these TSC phases, we find that the helical Majorana edge states become gapped, leading to the emergence of Majorana zero modes at specific corners of the system. The increase in the codimension of the Majorana modes on the boundary suggests a transition from first-order TSCs to second-order TSCs. Interestingly, the second-order TSC phases in this system can host not only isolated Majorana corner modes but also twofold Majorana corner modes, a feature enabled by the existence of the unconventional TSC phase supporting two pairs of helical Majorana edge states.

The rest of this paper is organized as follows. In Sec. II, we introduce the setup and Hamiltonian, and analyze the salient properties in the normal-state band structure. In Sec. III, we explore first-order TSC phases that can emerge in this system. In Sec. IV, we investigate the transition from first-order TSCs to second-order TSCs driven by an in-plane magnetic field. Finally, in Sec. V, we present a discussion and conclusions.

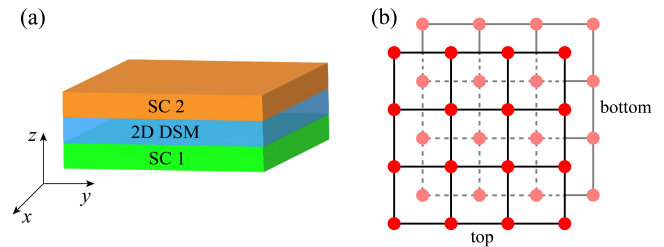


FIG. 1. (a) Schematic of the  $\pi$ -junction. The outer two materials are superconductors with even-parity  $s$ -wave or  $s_{\pm}$ -wave pairing, and the intermediate material is a 2D DSM. The two superconductors exhibit a  $\pi$  phase difference in their pairings. (b) Bilayer lattice structure of the 2D DSM.

## II. SETUP AND HAMILTONIAN

The setup concerned in this work is depicted in Fig.1(a). Specially, a 2D DSM is sandwiched between two superconductors with a  $\pi$  phase difference. The lattice structure of the 2D DSM is shown in Fig.1(b). It comprises two layers, which are shifted relative to each other by  $a(\frac{1}{2}, \frac{1}{2})$ , where  $a$  represents the lattice constants of the square lattice. We assume that each layer of the DSM inherits the same pairing type and phase from the fully-gapped superconductor in direct contact. The effective tight-binding Hamiltonian describing the superconducting DSM is given by  $H = \frac{1}{2} \sum_{\mathbf{k}} \Psi_{\mathbf{k}}^{\dagger} \mathcal{H}_{\text{BdG}}(\mathbf{k}) \Psi_{\mathbf{k}}$ , where the basis function is defined as  $\Psi_{\mathbf{k}}^{\dagger} = (c_{t,\uparrow,\mathbf{k}}^{\dagger}, c_{t,\downarrow,\mathbf{k}}^{\dagger}, c_{b,\uparrow,\mathbf{k}}^{\dagger}, c_{b,\downarrow,\mathbf{k}}^{\dagger}, c_{t,\uparrow,-\mathbf{k}}, c_{t,\downarrow,-\mathbf{k}}, c_{b,\uparrow,-\mathbf{k}}, c_{b,\downarrow,-\mathbf{k}})$ , and the Bogoliubov-de Gennes (BdG) Hamiltonian is expressed as

$$\mathcal{H}_{\text{BdG}}(\mathbf{k}) = \begin{pmatrix} \mathcal{H}_{\text{D}}(\mathbf{k}) - \mu & \Delta(\mathbf{k}) \\ \Delta^{\dagger}(\mathbf{k}) & -\mathcal{H}_{\text{D}}^T(-\mathbf{k}) + \mu \end{pmatrix}. \quad (1)$$

Here,  $\mathcal{H}_{\text{D}}(\mathbf{k})$  describes the band structure of the normal-state DSM,  $\mu$  is the chemical potential, and  $\Delta(\mathbf{k})$  is the pairing matrix. The explicit form of  $\mathcal{H}_{\text{D}}(\mathbf{k})$  is [95]

$$\mathcal{H}_{\text{D}}(\mathbf{k}) = -2t(\cos k_x + \cos k_y) + 4\eta \cos \frac{k_x}{2} \cos \frac{k_y}{2} \sigma_x + 2\lambda_{\text{so}}(\sin k_x \sigma_z s_y - \sin k_y \sigma_z s_x), \quad (2)$$

and the pairing matrix  $\Delta(\mathbf{k})$  is given by

$$\Delta(\mathbf{k}) = -i\sigma_z s_y [\Delta_0 + 2\Delta_1(\cos k_x + \cos k_y)]. \quad (3)$$

Here, the Pauli matrices  $\{\sigma_i\}$  and  $\{s_i\}$  act on the layer ( $t, b$ ) and spin ( $\uparrow, \downarrow$ ) degrees of freedom, respectively. In  $\mathcal{H}_{\text{D}}(\mathbf{k})$ , the parameter  $t$  represents the strength of the intralayer nearest-neighboring hopping,  $\eta$  denotes the strength of the interlayer nearest-neighboring hopping, and  $\lambda_{\text{so}}$  denotes the strength of SOC. For  $\Delta(\mathbf{k})$ ,  $\Delta_0$  denotes the on-site  $s$ -wave pairing amplitude, and  $\Delta_1$  represents the amplitude of the intralayer nearest-neighboring pairing. When  $\Delta_0$  is finite and  $\Delta_1$  vanishes, the pairing order parameter describes a conventional  $s$ -wave superconductor. When  $4|\Delta_1| > |\Delta_0|$ , the pairing order parameter has nodes in the Brillouin zone, and it

describes an  $s_{\pm}$ -wave superconductor if the pairing nodes lie between two Fermi surfaces of the superconductor. For notational simplicity, we set the lattice constant  $a$  to unity and omit the identity matrices in orbital and spin space throughout this work.

It is straightforward to verify that the DSM Hamiltonian  $\mathcal{H}_D(\mathbf{k})$  possesses the following symmetries [95]: time-reversal symmetry ( $\mathcal{T} = i s_y \mathcal{K}$  with  $\mathcal{K}$  the complex conjugate operator), inversion symmetry ( $\mathcal{P} = \sigma_x$ ), a glide mirror symmetry ( $\{\mathcal{M}_z | (\frac{1}{2}, \frac{1}{2})\}$  with  $\mathcal{M}_z = i \sigma_x s_z$ ) and two screw symmetries ( $\{\mathcal{C}_{2x} | (\frac{1}{2}, 0)\}$  and  $\{\mathcal{C}_{2y} | (0, \frac{1}{2})\}$  with  $\mathcal{C}_{2x} = i \sigma_x s_x$  and  $\mathcal{C}_{2y} = i \sigma_x s_y$ ). It is also straightforward to verify that the pairing is odd under inversion, satisfying  $\mathcal{P} \Delta(\mathbf{k}) \mathcal{P}^T = -\Delta(-\mathbf{k})$ . This suggests that the pairing form given in Eq.(3) describes an odd-parity spin-singlet pairing.

The symmetries in  $\mathcal{H}_D(\mathbf{k})$  guarantee the presence of four-fold degenerate Dirac points at the three time-reversal-invariant momenta:  $\mathbf{X} = (\pi, 0)$ ,  $\mathbf{Y} = (0, \pi)$  and  $\mathbf{M} = (\pi, \pi)$ . To see this more directly, we write down the energy spectra of the DSM, which read

$$\epsilon_{\pm}(\mathbf{k}) = \epsilon_0(\mathbf{k}) \pm \epsilon_1(\mathbf{k}), \quad (4)$$

where  $\epsilon_0(\mathbf{k}) = -2t(\cos k_x + \cos k_y)$  and  $\epsilon_1(\mathbf{k}) = \sqrt{(4\eta \cos \frac{k_x}{2} \cos \frac{k_y}{2})^2 + 4\lambda_{\text{so}}^2(\sin^2 k_x + \sin^2 k_y)}$ . Each band is doubly degenerate due to the simultaneous existence of time-reversal symmetry and inversion symmetry. It is evident that  $\epsilon_1(\mathbf{k})$  vanishes at  $\mathbf{X}$ ,  $\mathbf{Y}$  and  $\mathbf{M}$ . This results in four-fold band degeneracies at these time-reversal-invariant momenta, corresponding to the Dirac points, as illustrated in Fig.2(a).

Since superconductivity arises from an instability of the Fermi surface, the properties of the Fermi surface significantly influence the resulting superconducting phase. In the current system, the Fermi surfaces exhibit markedly different behaviors depending on whether they enclose a Dirac point. Specifically, when a segment of the Fermi surface encloses a Dirac point, it cannot be continuously deformed to vanish unless it merges with other Fermi surface segments that also enclose Dirac points. In contrast, when a Fermi surface segment does not enclose a Dirac point, it can be continuously deformed to vanish by tuning the parameters of the Hamiltonian. An illustration of the different evolution behaviors of these two types of Fermi surface segments as a function of chemical potential is presented in Figs.2(b) and 2(c). For clarity in the following discussion, we refer to Fermi surface segments that enclose a Dirac point as *Dirac Fermi surface segments* (DFSSs), and those that do not enclose a Dirac point as *normal Fermi surface segments* (NFSSs).

Several previous studies have demonstrated that the combination of this intriguing Dirac band structure with even-parity spin-singlet pairings can give rise to TSC phases with fascinating properties. Notably, since the DSM Hamiltonian also effectively describes the normal-state band structure of monolayer FeSe, an iron-based superconductor, Qin *et al.* showed that when the pairing is an  $s_{\pm}$ -wave pairing and its nodes lie between two DFSSs, a time-reversal-invariant second-order TSC emerges, hosting Majorana Kramers pairs at the system's corners [64]. In contrast, when the nodes lie between two

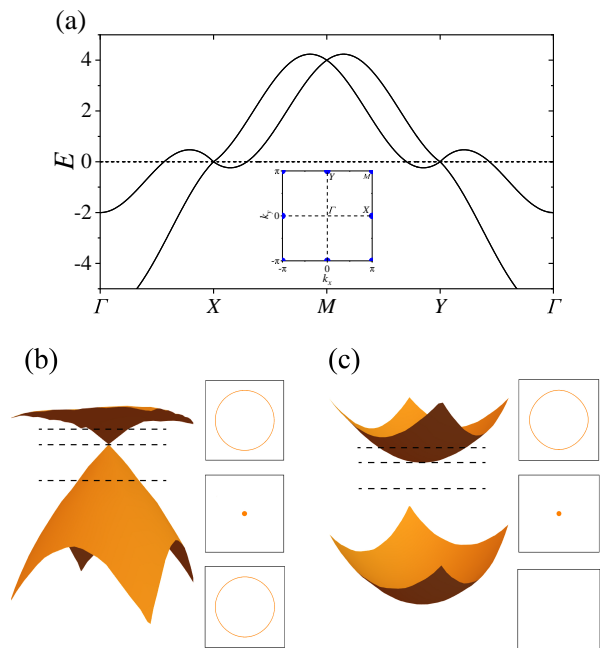


FIG. 2. (a) Representative band structure of the 2D DSM along high-symmetry lines. Dirac points are located at  $\mathbf{X} = (\pi, 0)$ ,  $\mathbf{Y} = (0, \pi)$  and  $\mathbf{M} = (\pi, \pi)$ . The inset depicts the 2D Brillouin zone, highlighting the four time-reversal invariant momenta and the locations of Dirac points (blue dots). (b) Evolution of a DFSS with  $\mu$ . Left panel shows the Dirac-cone band structure near  $\mathbf{M}$ . Right panels (top to bottom) show Fermi surface structures around  $\mathbf{M}$  for three different  $\mu$  marked by dashed lines. (c) Evolution of a NFSS with  $\mu$ . Left panel shows the band structure near the  $\Gamma = (0, 0)$  point. Right panels (top to bottom) show Fermi surface structures around  $\Gamma$  for three different  $\mu$  marked by dashed lines. The values of parameters are:  $t = 1$ ,  $\eta = 0.5$ , and  $\lambda_{\text{so}} = 0.5$ .

NFSSs, the resulting superconducting phase is topologically trivial. Furthermore, Mo *et al.* investigated  $s$ -wave superconductivity in this DSM and demonstrated that a perpendicular magnetic field can drive TSCs with large Chern numbers, as well as induce a nodal phase characterized by the coexistence of Bogoliubov Fermi surfaces and chiral Majorana edge states [101]. The study of odd-parity superconductivity in this DSM can serve as a complementary direction to these studies, offering additional insights into the rich TSC phases achievable in such systems.

### III. FIRST-ORDER TSC PHASES

#### A. General discussion of the topological characterization

Before proceeding to determine the possible TSC phases arising from odd-parity pairings, we first rewrite the BdG

Hamiltonian (1) in terms of Pauli matrices. This yields

$$\begin{aligned} \mathcal{H}_{\text{BdG}}(\mathbf{k}) = & [-2t(\cos k_x + \cos k_y) - \mu]\tau_z \\ & + 4\eta \cos \frac{k_x}{2} \cos \frac{k_y}{2} \tau_z \sigma_x \\ & + 2\lambda_{\text{so}}(\sin k_x \tau_z \sigma_z s_y - \sin k_y \sigma_z s_x) \\ & + [\Delta_0 + 2\Delta_1(\cos k_x + \cos k_y)]\tau_y \sigma_z s_y. \end{aligned} \quad (5)$$

Here, the Pauli matrices  $\{\tau_i\}$  act on the particle-hole space. For this BdG Hamiltonian, it possesses the following symmetries: time-reversal symmetry ( $\tilde{T} = i s_y \mathcal{K}$ ), inversion symmetry ( $\tilde{P} = \tau_z \sigma_x$ ), particle-hole symmetry ( $\Xi = \tau_x \mathcal{K}$ ), chiral symmetry ( $\mathcal{S} = \tau_x s_y$ ), the glide mirror symmetry ( $\{\tilde{\mathcal{M}}_z | (\frac{1}{2}, \frac{1}{2})\}$ ) with  $\tilde{\mathcal{M}}_z = i \sigma_x s_z$ , two screw symmetries ( $\{\tilde{\mathcal{C}}_{2x} | (\frac{1}{2}, 0)\}$ ) and ( $\{\tilde{\mathcal{C}}_{2y} | (0, \frac{1}{2})\}$ ) with  $\tilde{\mathcal{C}}_{2x} = i \sigma_x s_x$  and  $\tilde{\mathcal{C}}_{2y} = i \tau_z \sigma_x s_y$ .

Since this 2D superconducting system possesses time-reversal symmetry, particle-hole symmetry and chiral symmetry, it belongs to the DIII class and follows a  $Z_2$  classification according to the tenfold-way classification [98–100]. Because the inversion symmetry is also preserved and the pairing is of odd-parity nature, the  $Z_2$  invariant in the weak-pairing limit has a simple relation with the number of Kramers degenerate Fermi surface segments. Specially, the relation is given by [79]

$$(-1)^\nu = \prod_{i=1}^4 (-1)^{N(\mathbf{K}_i)}, \quad (6)$$

where  $\mathbf{K}_i \in \{\Gamma, \mathbf{X}, \mathbf{Y}, \mathbf{M}\}$  represents a time-reversal-invariant momentum, and  $N(\mathbf{K}_i)$  denotes the number of Fermi surface segments that enclose  $\mathbf{K}_i$ . The simple formula (6) reveals that when the total number of Fermi surface segments is odd, the system is  $Z_2$  nontrivial and realizes a helical TSC. This phase is characterized by a pair of helical Majorana edge states protected by time-reversal symmetry. In contrast, when the total number of Fermi surface segments is even, the system is  $Z_2$  trivial, and robust helical Majorana edge states are absent unless additional topological classifications emerge from further symmetry protections [102–104].

In the current system, glide mirror symmetry introduces an additional topological classification. Since the mirror operator  $\tilde{\mathcal{M}}_z$  commutes with the BdG Hamiltonian,  $[\tilde{\mathcal{M}}_z, \mathcal{H}_{\text{BdG}}(\mathbf{k})] = 0$ , the Hamiltonian  $\mathcal{H}_{\text{BdG}}(\mathbf{k})$  becomes block diagonal in the basis where  $\tilde{\mathcal{M}}_z$  takes the diagonal form  $\text{diag}\{iI_{4 \times 4}, -iI_{4 \times 4}\}$ . Here  $I_{4 \times 4}$  represents the  $4 \times 4$  identity matrix. The block diagonal form of  $\mathcal{H}_{\text{BdG}}(\mathbf{k})$  can be expressed as  $\mathcal{H}_{\text{BdG}}(\mathbf{k}) = \mathcal{H}_{+i}(\mathbf{k}) \oplus \mathcal{H}_{-i}(\mathbf{k})$ , where the subscript  $+i$  ( $-i$ ) indicates that the block corresponds to the positive (negative) eigenvalue of the mirror operator. The explicit forms of the Hamiltonians for the two mirror sectors are given

by

$$\begin{aligned} \mathcal{H}_{\pm i}(\mathbf{k}) = & [-2t(\cos k_x + \cos k_y) - \mu]\tau_z \\ & + 4\eta \cos \frac{k_x}{2} \cos \frac{k_y}{2} \tau_z \rho_z \\ & - 2\lambda_{\text{so}}(\pm \sin k_x \tau_z \rho_y - \sin k_y \rho_x) \\ & \mp [\Delta_0 + 2\Delta_1(\cos k_x + \cos k_y)]\tau_y \rho_y. \end{aligned} \quad (7)$$

Here,  $\{\rho_i\}$  denotes a new set of Pauli matrices that act on degrees of freedom arising from a combination of the layer and spin degrees of freedom. It is straightforward to verify that the Hamiltonians for both mirror sectors preserve the particle-hole symmetry. However, time-reversal symmetry and chiral symmetry are broken. Therefore, each mirror-sector Hamiltonian belongs to the D class and follows a  $Z$  classification according to the tenfold-way classification [98–100]. The corresponding  $Z$ -valued topological invariant is the Chern number, defined as [105]

$$C_{\pm i} = \frac{1}{2\pi} \sum_n \int_{BZ} \Omega_{\pm i}^{(n)}(\mathbf{k}) d\mathbf{k}, \quad (8)$$

where  $\Omega_{\pm i}^{(n)}$  denotes the Berry curvature of the  $n$ th negative energy band in the  $\pm i$  mirror-sector Hamiltonian, and the summation is taken over all negative energy bands. Since the full Hamiltonian possesses time-reversal symmetry, the total Chern number, which is the summation of the Chern numbers of the two mirror-sector Hamiltonians, is constrained by symmetry to vanish identically. This also implies that the Chern numbers for the two mirror sectors satisfy the relation  $C_{+i} = -C_{-i}$ . Consequently, if one mirror sector hosts  $n$  branches of chiral Majorana edge states, the other mirror sector must also support  $n$  branches of chiral Majorana edge states, but with opposite chirality. Together, these form  $n$  pairs of helical Majorana edge states. As a result, the relevant topological invariant in this context is the mirror Chern number, defined as [106]

$$C_M = \frac{1}{2}(C_{+i} - C_{-i}). \quad (9)$$

This invariant extends the topological classification from a  $Z_2$  classification to a  $Z$  classification and enables the presence of multiple pairs of robust helical Majorana edge modes. When the mirror Chern number  $C_M$  is nonzero, the resulting phase is also referred to as a topological mirror superconductor [107]. Since the set of possible values for  $\nu$  is a subset of those for  $C_M$ , we will primarily use  $C_M$  to diagnose the topological classification of the resulting superconducting phases.

## B. First-order TSC phases in the $\pi$ -junction formed by $s$ -wave superconductors

We first focus on the case where  $\Delta_0$  is finite and  $\Delta_1$  vanishes. Since the change of first-order topology must be accompanied by the closing of bulk energy gap, we determine the gap-closing condition for this scenario. From Eq.(5), the energy spectra can be directly derived as

$$E_{\alpha\beta}(\mathbf{k}) = \alpha\sqrt{\xi^2(\mathbf{k}) + \eta^2(\mathbf{k}) + \Lambda^2(\mathbf{k}) + \Delta_0^2} + 2\beta\sqrt{\xi^2(\mathbf{k})(\eta^2(\mathbf{k}) + \Lambda^2(\mathbf{k})) + \Delta_0^2\eta^2(\mathbf{k})}, \quad (10)$$

where  $\alpha$  and  $\beta$  take values in  $\{+, -\}$ , and we have introduced the short-hand notations:  $\xi(\mathbf{k}) = -2t(\cos k_x + \cos k_y) - \mu$ ,  $\eta(\mathbf{k}) = 4\eta \cos(k_x/2) \cos(k_y/2)$ , and  $\Lambda(\mathbf{k}) = 2\lambda_{\text{so}}\sqrt{\sin^2 k_x + \sin^2 k_y}$ . The energy gap can only close at the four time-reversal invariant momenta where the parameter  $\Lambda(\mathbf{k})$  vanishes identically. Based on this observation, the gap-closing condition can be readily derived as [20]

$$\eta(\mathbf{K}_i) = \pm\sqrt{\xi^2(\mathbf{K}_i) + \Delta_0^2}. \quad (11)$$

Since  $\eta(\mathbf{K}_i)$  vanishes when  $\mathbf{K}_i = (0, \pi)$ ,  $(\pi, 0)$  and  $(\pi, \pi)$ , the above equation can be satisfied only at the time-reversal invariant momentum  $(0, 0)$ . At this point, the condition is concretized as

$$4\eta = \pm\sqrt{(4t + \mu)^2 + \Delta_0^2}. \quad (12)$$

To simplify the discussion, we restrict our analysis to the case where  $\eta$  and  $t$  are positive parameters. Furthermore, we assume that  $\mu$  is the only tuning parameter and that  $4\eta > |\Delta_0|$ , ensuring that gap closure can occur. Under these assumptions, Eq. (12) shows that the bulk energy gap closes when the chemical potential  $\mu$  takes the following critical values:  $\mu_1 = -4t - \sqrt{16\eta^2 - \Delta_0^2}$  and  $\mu_2 = -4t + \sqrt{16\eta^2 - \Delta_0^2}$ . To determine the topological phase diagram, we note that the system must be topologically trivial in the limit  $\mu \rightarrow -\infty$  (where all bands in the normal state are empty) and in the limit  $\mu \rightarrow +\infty$  (where all bands in the normal state are occupied). By applying the adiabatic principle—which states that the first-order topology remains unchanged as long as the change of parameters does not induce the closing of the bulk energy gap—we conclude that the system can only be topologically nontrivial when  $\mu_1 < \mu < \mu_2$ . Numerical calculations confirm this analysis, showing that the mirror Chern number  $C_M$  equals  $-1$  within this range and zero otherwise, as shown in Fig. 3(a).

In the weak-pairing limit, i.e.,  $|\Delta_0| \ll \eta$  and  $|\Delta_0| \ll t$ , we find that within the topological region, there is only a single Fermi surface segment. In contrast, in the trivial regions, the number of Fermi surface segments is even, as illustrated by the insets in Fig. 3(a). From Eq.(6), we know that the  $Z_2$  invariant  $\nu$  equals 1 when a single Fermi surface segment exists, and 0 when the number of Fermi surface segments is even. This demonstrates the consistency between the mirror Chern number  $C_M$  and the  $Z_2$  invariant  $\nu$ .

In Figs. 3(b) and 3(c), we present the energy spectra of the system under open boundary conditions in the  $x$  direction and periodic boundary conditions in the  $y$  direction. Fig. 3(b) corresponds to the system being in the topological region, where we observe a pair of helical Majorana edge states traversing the bulk energy gap. In contrast, Fig. 3(c) illustrates the trivial region, where no edge states are present within the bulk energy gap. The presence or absence of helical Majorana

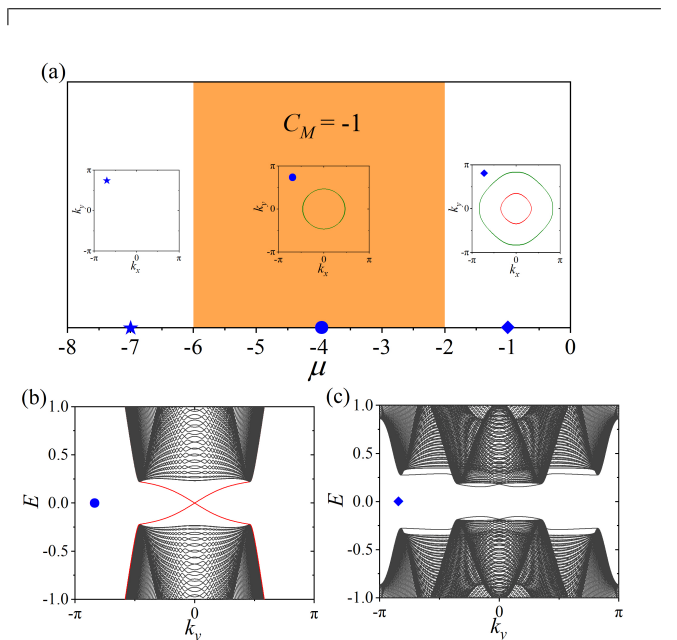


FIG. 3. (a) Topological phase diagram determined by the mirror Chern number. Insets (left to right) show the Fermi surface structures corresponding to  $\mu$  marked by star, dot and diamond, respectively. The two pairing parameters are set to  $\Delta_0 = 0.1$  and  $\Delta_1 = 0$ . In (b) and (c), energy spectra for a system with periodic (open) boundary conditions in the  $y$  ( $x$ ) direction are shown. In (b),  $\mu = -4$ , a pair of helical Majorana modes (red lines) appears within the energy gap, consistent with the mirror Chern number  $C_M = -1$ . In (c),  $\mu = -1$ , no mid-gap states exist, consistent with  $C_M = 0$ . In (b) and (c), the two pairing parameters are set to  $\Delta_0 = 0.4$  and  $\Delta_1 = 0$ . A larger value of  $\Delta_0$  is chosen to more clearly highlight the edge states within the energy gap. The values of other parameters are:  $t = 1$ ,  $\eta = 0.5$ , and  $\lambda_{\text{so}} = 0.5$ .

edge states, as well as their number, is fully consistent with the topological invariant.

To conclude this section, we find that when a  $\pi$ -junction is formed between two  $s$ -wave superconductors, only one first-order TSC phase exists. This phase is characterized by the  $Z_2$  invariant  $\nu = 1$  and the mirror Chern number  $C_M = -1$ , and is manifested by the presence of a pair of helical Majorana edge states localized at the boundary.

### C. First-order TSC phases in the $\pi$ -junction formed by $s_{\pm}$ -wave superconductors

We now investigate the TSC phases that can arise in a  $\pi$ -junction formed by two  $s_{\pm}$ -wave superconductors. The key distinction between the odd-parity pairing induced by  $s$ -wave superconductors and that induced by  $s_{\pm}$ -wave superconductors lies in the presence or absence of pairing nodes. As

previously mentioned, Qin *et al.* demonstrated that when the pairing nodes of an even-parity  $s_{\pm}$ -wave pairing are located between two DFSSs, the system realizes a time-reversal-invariant second-order TSC phase characterized by the presence of Majorana corner modes [64]. In contrast, when the pairing nodes lie between two NFSSs, the system becomes a trivial superconductor. This insight motivates us to explore analogous configurations in the present context to determine whether similar or distinct behaviors emerge.

To construct the topological phase diagram, we first determine the gap-closing conditions. We assume that the chemical potential  $\mu$  is the only variable, while the parameters  $t$ ,  $\eta$ ,  $\lambda_{\text{so}}$  and  $\Delta_1$  are held fixed as positive constants. Under these assumptions, we find that the energy gap closes under the following conditions:

(I)  $|\Delta_0| > 4\Delta_1$  (no pairing nodes; energy gap closes at high symmetry points).

In this regime, the energy gap closes only at the  $\Gamma$  point when  $\mu$  takes one of the following two values:

$$\begin{aligned}\mu'_1 &= -4t - \sqrt{16\eta^2 - (\Delta_0 + 4\Delta_1)^2}, \\ \mu'_2 &= -4t + \sqrt{16\eta^2 - (\Delta_0 + 4\Delta_1)^2}.\end{aligned}\quad (13)$$

(II)  $0 < \Delta_0 < 4\Delta_1$  (pairing nodes enclose the  $M$  point; energy gap closes at points of high symmetry lines).

For this case, the energy gap can close not only at the  $\Gamma$  point (with  $\mu$  given by Eq.(13)), but also at the Brillouin zone boundary. To illustrate this, we note that the parameter  $\eta(\mathbf{k})$  vanishes when  $k_x = \pi$  or  $k_y = \pi$ . Focusing on the line  $k_x = \pi$ , the energy spectrum simplifies to  $E_{\pm, \pm}(\pi, k_y) = \pm\sqrt{\xi_{\pm}^2(k_y) + \Delta^2(k_y)}$ , where  $\xi_{\pm}(k_y) = -2t(\cos k_y - 1) - \mu \pm 2\lambda_{\text{so}} \sin k_y$  and  $\Delta(k_y) = \Delta_0 + 2\Delta_1(\cos k_y - 1)$ . The energy gap closes at  $k_y = \pm \arccos\left(\frac{2\Delta_1 - \Delta_0}{2\Delta_1}\right)$  when  $\mu$  takes the values:

$$\begin{aligned}\mu'_3 &= \frac{t\Delta_0}{\Delta_1} - 2\lambda_{\text{so}}\sqrt{1 - \left(\frac{\Delta_0 - 2\Delta_1}{2\Delta_1}\right)^2}, \\ \mu'_4 &= \frac{t\Delta_0}{\Delta_1} + 2\lambda_{\text{so}}\sqrt{1 - \left(\frac{\Delta_0 - 2\Delta_1}{2\Delta_1}\right)^2}.\end{aligned}\quad (14)$$

Similarly, along the line  $k_y = \pi$ , the energy gap closes at  $k_x = \pm \arccos\left(\frac{2\Delta_1 - \Delta_0}{2\Delta_1}\right)$  for the same values of  $\mu$  given in Eq.(14).

(III)  $|\Delta_0| < 4\Delta_1$  (pairing nodes present; energy gap closes at generic points).

When pairing nodes are present, the energy gap can also close at generic points in the Brillouin zone that simultaneously satisfy

$$\begin{aligned}\Delta_0 + 2\Delta_1(\cos k_x + \cos k_y) &= 0, \\ \xi(\mathbf{k}) \pm \sqrt{\eta^2(\mathbf{k}) + \Lambda^2(\mathbf{k})} &= 0.\end{aligned}\quad (15)$$

Since these solutions correspond to generic points in the Brillouin zone, analytical expressions for the critical values of  $\mu$  cannot be obtained. Nevertheless, the gap-closing conditions can be determined numerically.

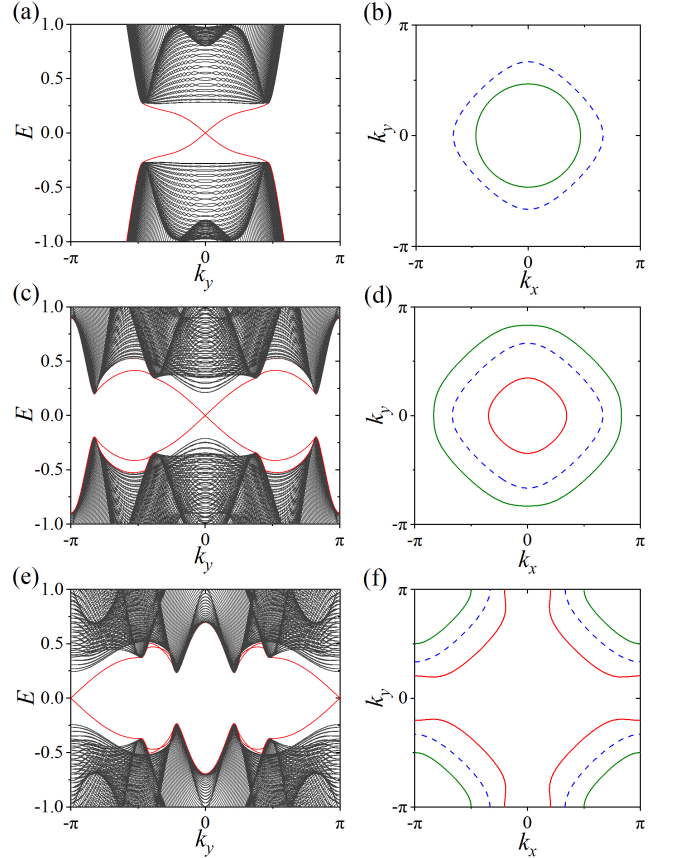


FIG. 4. Left panels: Energy spectra for a system with periodic (open) boundary conditions in the  $y$  ( $x$ ) direction. Right panels: Fermi surface structure (solid lines) and pairing nodes (dash lines) correspond to the left panels. From top to bottom, parameters  $\{\mu, \Delta_0, \Delta_1\}$  are set as  $\{-4, -0.4, 0.4\}$ ,  $\{-1, -0.4, 0.4\}$ , and  $\{1, 0.4, 0.4\}$ , respectively. The values of other parameters are:  $t = 1$ ,  $\eta = 0.5$ , and  $\lambda_{\text{so}} = 0.5$ .

By numerically calculating the mirror Chern number  $C_M$ , we find that it changes value only when the energy gap closes at the  $\Gamma$  point. This behavior is identical to the previous case where the  $\pi$ -junction is formed by  $s$ -wave superconductors. Specially, we obtain  $C_M = -1$  for  $\mu'_1 < \mu < \mu'_2$ , corresponding to a regime with a single Fermi surface segment in the weak-pairing limit. Outside this range,  $C_M = 0$ , and the number of Fermi surface segments is even.

In the region where only a Fermi surface segment exists and  $C_M = -1$ , a pair of helical Majorana edge states is also observed to appear within the bulk energy gap, as shown in Figs.4(a) and 4(b). Interestingly, when the system has two Fermi surface segments and the pairing nodes lie between them, we find two pairs of robust helical Majorana edge states, even though both the mirror Chern number  $C_M$  and the  $Z_2$  invariant are zero. Notably, these helical Majorana edge states emerge regardless of whether the two Fermi surface segments are DFSSs or NFSSs, as illustrated in Figs.4(c)-4(f). This behavior is markedly distinct from the even-parity pairing case, where nontrivial topology emerges exclusively when the pair-

ing nodes lie between two DFSSs [64].

How can we understand the presence of two pairs of robust helical Majorana edge states when the mirror Chern number  $C_M$  is zero? We find that this phenomenon can be explained using weak topological invariants defined along the high-symmetry lines of the Brillouin zone [83]. Specifically, we note that while each mirror-sector Hamiltonian belongs to the D class, the reduced 1D Hamiltonian along these high-symmetry lines exhibits an emergent chiral symmetry, placing it in the BDI class [98–100]. The BDI class, characterized by higher symmetry, follows a  $Z$  classification in 1D. To illustrate this, consider the two mirror-sector Hamiltonians along the line  $k_y = 0$ ,

$$\begin{aligned} \mathcal{H}_{\pm i}(k_x, 0) &= [-2t(\cos k_x + 1) - \mu]\tau_z \\ &+ 4\eta \cos \frac{k_x}{2} \tau_z \rho_z \mp 2\lambda_{\text{so}} \sin k_x \tau_z \rho_y \\ &\mp [\Delta_0 + 2\Delta_1(\cos k_x + 1)]\tau_y \rho_y. \end{aligned} \quad (16)$$

It is straightforward to verify that these two reduced 1D Hamiltonians possess chiral symmetry, with the chiral operator given by  $\mathcal{S}_0 = \tau_x$ . Similarly, the two mirror-sector Hamiltonians along the line  $k_y = \pi$  take the form

$$\begin{aligned} \mathcal{H}_{\pm i}(k_x, \pi) &= [-2t(\cos k_x - 1) - \mu]\tau_z \mp 2\lambda_{\text{so}} \sin k_x \tau_z \rho_y \\ &\mp [\Delta_0 + 2\Delta_1(\cos k_x - 1)]\tau_y \rho_y, \end{aligned} \quad (17)$$

which also possess chiral symmetry, with  $\mathcal{S}_\pi = \tau_x$ . The band topology of these 1D Hamiltonians is characterized by a winding number, defined as [100]

$$\begin{aligned} W_{\pm i}^{0/\pi} &= \frac{1}{4\pi i} \oint dk_x \text{Tr}[\mathcal{S}_{0/\pi} H_{\pm i}^{-1}(k_x, k_y = 0/\pi) \\ &\times \partial_{k_x} H_{\pm i}(k_x, k_y = 0/\pi)]. \end{aligned} \quad (18)$$

Here,  $W_{\pm i}^0$  and  $W_{\pm i}^\pi$  quantify the number of Majorana zero modes per boundary at  $k_y = 0$  and  $k_y = \pi$ , respectively. Through numerical calculations, we find that the mirror-graded winding number  $W_{\pm i}^0$  equals  $-2$  for the configuration of pairing nodes and Fermi surfaces shown in Fig.4(d). The combination of  $C_{\pm i} = 0$  and  $W_{\pm i}^0 = -2$  implies the presence of a pair of helical Majorana edge states in each mirror sector. Furthermore,  $W_{\pm i}^0 = -2$  indicates the presence of four Majorana zero modes per boundary when  $k_y = 0$ , corresponding to an eightfold crossing of the edge states' spectrum at  $E = 0$  and  $k_y = 0$ , as shown in Fig.4(c). Similarly, the combination of  $C_{\pm i} = 0$  and  $W_{\pm i}^\pi = 2$  also suggests the presence of a pair of helical Majorana edge states in each mirror sector. Additionally,  $W_{\pm i}^\pi = 2$  indicates that the edge states' spectrum crosses at  $E = 0$  occurs when  $k_y = \pi$ , as shown in Fig.4(e).

A combination of  $C_M$  and  $W_{\pm i}^{0/\pi}$  provides a comprehensive understanding of the topology of the resulting superconducting phases. A representative topological phase diagram based on these invariants is shown in Fig. 5(a). Within the topological phase diagram, the TSC phase characterized by  $C_M = -1$  and  $W_{\pm i}^0 = 1$  hosts one chiral Majorana edge state in each mirror sector. Furthermore, the chiral Majorana edge states in the two mirror sectors exhibit opposite chirality, as illustrated

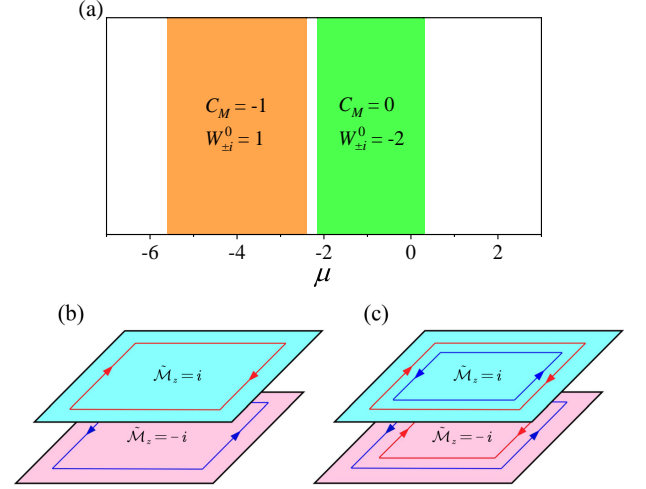


FIG. 5. (a) Representative topological phase diagram determined by the mirror Chern number  $C_M$  and the weak topological invariants  $W_{\pm i}^0$ . The parameter values are:  $t = 1$ ,  $\eta = 0.5$ , and  $\lambda_{\text{so}} = 0.5$ ,  $\Delta_0 = -0.4$  and  $\Delta_1 = 0.4$ . For this set of parameters,  $W_{\pm i}^\pi$  vanish identically and is therefore not considered. (b) Schematic of the edge states for the TSC phase characterized by  $C_M = -1$  and  $W_{\pm i}^0 = 1$ . (c) Schematic of the edge states for the TSC phase characterized by  $C_M = 0$  and  $W_{\pm i}^0 = -2$ .

in Fig. 5(b). On the other hand, the TSC phase characterized by  $C_M = 0$  and  $W_{\pm i}^0 = -2$  (or  $W_{\pm i}^\pi = 2$ ) hosts one pair of helical Majorana edge state in each mirror sector, as illustrated in Fig. 5(c).

#### IV. SECOND-ORDER TSC PHASES

As previously mentioned, a transition from time-reversal-invariant first-order TSC phases to a time-reversal-symmetry-broken second-order TSC phase can be induced by applying an in-plane magnetic field. Previous studies have demonstrated that gapping out one pair of helical Majorana edge states can lead to the emergence of isolated Majorana zero modes at specific corners of an open-boundary system [34, 38]. In our system, a TSC phase with two pairs of helical Majorana edge states exists, which suggests the possibility of observing twofold Majorana zero modes at the corners [59, 108]. To investigate this, we introduce an in-plane magnetic field, which induces a Zeeman field described by  $\mathcal{H}_Z = M_x \tau_z s_x + M_y s_y$  into the BdG Hamiltonian (5). This Zeeman field breaks both time-reversal symmetry and glide mirror symmetry, resulting in a coupling between the chiral or helical Majorana edge states in the two mirror sectors.

Specifically, we consider a system with open boundary conditions in both the  $x$  and  $y$  directions, subjected to a Zeeman field aligned along either the diagonal or anti-diagonal direction. By computing the energy spectrum, we observe that the helical Majorana edge states are gapped, leaving only two or four zero-energy states within the spectral gap. As expected, the number of these zero-energy states is directly tied to the

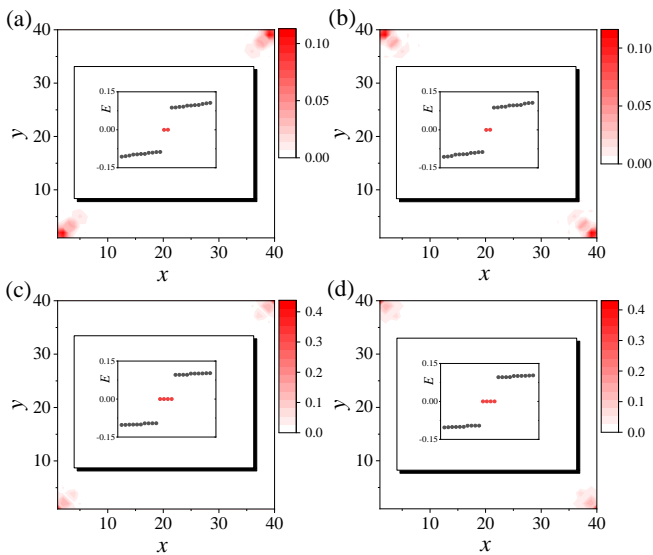


FIG. 6. Probability density profiles of Majorana corner modes in an open boundary system of size  $N_x \times N_y = 40 \times 40$ . Insets show a few eigenenergies closest to  $E = 0$ . Parameters  $\{\mu, \Delta_0, \Delta_1\}$  are set as  $\{-4, -0.4, 0.4\}$  and  $\{1, 0.4, 0.4\}$  for the top and bottom panels, respectively. Parameters  $\{M_x, M_y\}$  are chosen as  $\{0.1, 0.1\}$  and  $\{0.1, -0.1\}$  for the left and right panels, respectively. The top (bottom) two panels show the presence of isolated (twofold) Majorana corner modes at two of the four corners. The values of other parameters are:  $t = 1$ ,  $\eta = 0.5$ , and  $\lambda_{\text{so}} = 0.5$ .

number of helical Majorana edge state. These mid-gap states are identified as Majorana zero modes, and their wave functions are strongly localized at two inversion-related corners. Notably, the positions of these Majorana zero modes are determined by the orientation of the Zeeman field. This implies that the direction of the magnetic field can be used to control their locations, as illustrated in Fig. 6. These results suggest that this setup provides a practical platform for realizing highly tunable multifold Majorana corner modes.

In a superconductor, chiral symmetry arises from the coexistence of time-reversal symmetry and particle-hole symmetry. Therefore, breaking time-reversal symmetry with a magnetic field typically implies the absence of chiral symmetry. In the absence of chiral symmetry, Majorana zero modes generally follow a  $Z_2$  classification [98–100]. A consequence of this is that two spatially overlapping Majorana zero modes will hybridize, causing their energies to split from zero to finite values. In our system, although the spinful time-reversal symmetry and glide mirror symmetry are broken by the magnetic field, we find that their combination remains invariant. This invariance gives rise to an effective spinless time-reversal symmetry, with the symmetry operator given by  $\mathcal{T}' = -i\tilde{\mathcal{T}}\mathcal{M}_z = \sigma_x s_x \mathcal{K}$ . This operator satisfies  $(\mathcal{T}')^2 = 1$  and  $\mathcal{T}'\mathcal{H}'_{\text{BdG}}(\mathbf{k})(\mathcal{T}')^{-1} = \mathcal{H}'_{\text{BdG}}(-\mathbf{k})$ , where  $\mathcal{H}'_{\text{BdG}}(\mathbf{k}) = \mathcal{H}_{\text{BdG}}(\mathbf{k}) + \mathcal{H}_Z$ . The combination of this effective time-reversal symmetry and particle-hole symmetry results in an effective chiral symmetry, with the symmetry operator given by  $\mathcal{S}' = \tau_x \sigma_x s_x$ . This symmetry ensures the

stability of the twofold Majorana corner modes [108, 109], protecting them from hybridization and energy splitting.

## V. DISCUSSIONS AND CONCLUSIONS

Since even-parity pairings are ubiquitous in real materials, while odd-parity pairings are rare, inducing odd-parity superconductivity in carefully designed structures based on even-parity superconductors offers a promising alternative pathway to explore unique phases associated with odd-parity superconductivity. The  $\pi$ -junction formed by even-parity superconductors offers a practical pathway for inducing odd-parity pairings in bilayer and thin-film systems. Notably, this mechanism preserves time-reversal symmetry, thereby enabling the realization of time-reversal-invariant TSC phases. In this work, we show that when a 2D DSM is sandwiched between two  $s$ -wave or  $s_{\pm}$ -wave superconductors with a  $\pi$  phase difference in their pairings, time-reversal-invariant first-order TSCs characterized by a pair of helical Majorana edge states can be achieved when the system has only a Fermi surface segment in the normal state. Additionally, we identify an unconventional TSC phase characterized by two pairs of helical Majorana edge states when the pairing nodes lie between two Fermi surface segments, even though the bulk topological invariants, such as the mirror Chern number and the  $Z_2$  invariant, take the trivial value. The robustness of two pairs of helical Majorana edge states can be attributed to weak topological invariants defined along high symmetry lines within the Brillouin zone. Interestingly, applying an in-plane magnetic field can gap out these helical Majorana edge states, leading to the emergence of Majorana corner states. Due to the presence of an effective chiral symmetry, we demonstrate that this system can host not only isolated Majorana corner modes but also twofold Majorana corner modes.

To date, a variety of materials have been predicted to host Dirac points within their band structures such as black phosphorus [110], FeSe [111],  $X_3\text{SiTe}_6$  ( $X = \text{Ta}, \text{Nb}$ ) [112, 113], SbSSn [114],  $\text{HfGe}_{0.92}\text{Te}$  [115], and others [116]. Furthermore, the  $\pi$  phase difference in pairings can be controlled using SQUID technology, which is well-established. These material candidates, combined with the advanced control over phase differences, provide a solid foundation for realizing our proposed systems. As a final remark, interaction-driven odd-parity pairing could, in principle, also arise in this metallic system, just similar to previous studies [84–86]. We leave the exploration of this scenario for future work.

In conclusion, our work demonstrates that  $\pi$ -junction DSMs can support a rich variety of TSCs, ranging from first-order to second-order TSC phases. This offers a versatile platform for exploring exotic topological phenomena and advancing the field of topological superconductivity.

## ACKNOWLEDGEMENTS

This work is supported by the National Natural Science Foundation of China (Grant No.12174455) and Guangdong



- [1] X.-L. Qi and S.-C. Zhang, Topological insulators and superconductors, *Rev. Mod. Phys.* **83**, 1057 (2011).
- [2] J. Alicea, New directions in the pursuit of majorana fermions in solid state systems, *Reports on Progress in Physics* **75**, 076501 (2012).
- [3] M. Leijnse and K. Flensberg, Introduction to topological superconductivity and majorana fermions, *Semiconductor Science and Technology* **27**, 124003 (2012).
- [4] Y. Tanaka, M. Sato, and N. Nagaosa, Symmetry and Topology in Superconductors –Odd-Frequency Pairing and Edge States–, *Journal of the Physical Society of Japan* **81**, 011013 (2012).
- [5] T. D. Stanescu and S. Tewari, Majorana fermions in semiconductor nanowires: fundamentals, modeling, and experiment, *Journal of Physics: Condensed Matter* **25**, 233201 (2013).
- [6] C. W. J. Beenakker, Search for Majorana Fermions in Superconductors, *Annual Review of Condensed Matter Physics* **4**, 113 (2013).
- [7] S. R. Elliott and M. Franz, *Colloquium* : Majorana fermions in nuclear, particle, and solid-state physics, *Rev. Mod. Phys.* **87**, 137 (2015).
- [8] M. Sato and S. Fujimoto, Majorana fermions and topology in superconductors, *Journal of the Physical Society of Japan* **85**, 072001 (2016).
- [9] C. Nayak, S. H. Simon, A. Stern, M. Freedman, and S. Das Sarma, Non-Abelian anyons and topological quantum computation, *Rev. Mod. Phys.* **80**, 1083 (2008).
- [10] S. D. Sarma, M. Freedman, and C. Nayak, Majorana zero modes and topological quantum computation, *npj Quantum Information* **1**, 15001 (2015).
- [11] T. Karzig, C. Knapp, R. M. Lutchyn, P. Bonderson, M. B. Hastings, C. Nayak, J. Alicea, K. Flensberg, S. Plugge, Y. Oreg, C. M. Marcus, and M. H. Freedman, Scalable designs for quasiparticle-poisoning-protected topological quantum computation with Majorana zero modes, *Phys. Rev. B* **95**, 235305 (2017).
- [12] P. Marra, Majorana nanowires for topological quantum computation, *Journal of Applied Physics* **132**, 231101 (2022).
- [13] N. Read and D. Green, Paired states of fermions in two dimensions with breaking of parity and time-reversal symmetries and the fractional quantum hall effect, *Phys. Rev. B* **61**, 10267 (2000).
- [14] A. Y. Kitaev, Unpaired Majorana fermions in quantum wires, *Physics-Uspekhi* **44**, 131 (2001).
- [15] X.-L. Qi, T. L. Hughes, S. Raghu, and S.-C. Zhang, Time-reversal-invariant topological superconductors and superfluids in two and three dimensions, *Phys. Rev. Lett.* **102**, 187001 (2009).
- [16] C. Kallin and J. Berlinsky, Chiral superconductors, *Reports on Progress in Physics* **79**, 054502 (2016).
- [17] L. Fu and C. L. Kane, Superconducting Proximity Effect and Majorana Fermions at the Surface of a Topological Insulator, *Phys. Rev. Lett.* **100**, 096407 (2008).
- [18] C. Zhang, S. Tewari, R. M. Lutchyn, and S. Das Sarma,  $p_x + ip_y$  Superfluid from  $s$ -Wave Interactions of Fermionic Cold Atoms, *Phys. Rev. Lett.* **101**, 160401 (2008).
- [19] M. Sato, Y. Takahashi, and S. Fujimoto, Non-Abelian Topological Order in  $s$ -Wave Superfluids of Ultracold Fermionic Atoms, *Phys. Rev. Lett.* **103**, 020401 (2009).
- [20] J. D. Sau, R. M. Lutchyn, S. Tewari, and S. Das Sarma, Generic New Platform for Topological Quantum Computation Using Semiconductor Heterostructures, *Phys. Rev. Lett.* **104**, 040502 (2010).
- [21] J. Alicea, Majorana fermions in a tunable semiconductor device, *Phys. Rev. B* **81**, 125318 (2010).
- [22] R. M. Lutchyn, J. D. Sau, and S. Das Sarma, Majorana Fermions and a Topological Phase Transition in Semiconductor-Superconductor Heterostructures, *Phys. Rev. Lett.* **105**, 077001 (2010).
- [23] Y. Oreg, G. Refael, and F. von Oppen, Helical liquids and majorana bound states in quantum wires, *Phys. Rev. Lett.* **105**, 177002 (2010).
- [24] V. Mourik, K. Zuo, S. M. Frolov, S. R. Plissard, E. P. A. M. Bakkers, and L. P. Kouwenhoven, Signatures of majorana fermions in hybrid superconductor-semiconductor nanowire devices, *Science* **336**, 1003 (2012).
- [25] S. Nadj-Perge, I. K. Drozdov, J. Li, H. Chen, S. Jeon, J. Seo, A. H. MacDonald, B. A. Bernevig, and A. Yazdani, Observation of majorana fermions in ferromagnetic atomic chains on a superconductor, *Science* **346**, 602 (2014).
- [26] H.-H. Sun, K.-W. Zhang, L.-H. Hu, C. Li, G.-Y. Wang, H.-Y. Ma, Z.-A. Xu, C.-L. Gao, D.-D. Guan, Y.-Y. Li, C. Liu, D. Qian, Y. Zhou, L. Fu, S.-C. Li, F.-C. Zhang, and J.-F. Jia, Majorana zero mode detected with spin selective andreev reflection in the vortex of a topological superconductor, *Phys. Rev. Lett.* **116**, 257003 (2016).
- [27] D. Wang, L. Kong, P. Fan, H. Chen, S. Zhu, W. Liu, L. Cao, Y. Sun, S. Du, J. Schneeloch, *et al.*, Evidence for majorana bound states in an iron-based superconductor, *Science* **362**, 333 (2018).
- [28] L. Kong, S. Zhu, M. Papaj, H. Chen, L. Cao, H. Isobe, Y. Xing, W. Liu, D. Wang, P. Fan, Y. Sun, S. Du, J. Schneeloch, R. Zhong, G. Gu, L. Fu, H.-J. Gao, and H. Ding, Half-integer level shift of vortex bound states in an iron-based superconductor, *Nature Physics* **15**, 1181 (2019).
- [29] A. Fornieri, A. M. Whiticar, F. Setiawan, E. Portolés, A. C. C. Drachmann, A. Keselman, S. Gronin, C. Thomas, T. Wang, R. Kallaher, G. C. Gardner, E. Berg, M. J. Manfra, A. Stern, C. M. Marcus, and F. Nichele, Evidence of topological superconductivity in planar josephson junctions, *Nature* **569**, 89 (2019).
- [30] H. Ren, F. Pientka, S. Hart, A. T. Pierce, M. Kosowsky, L. Lunczer, R. Schlereth, B. Scharf, E. M. Hankiewicz, L. W. Molenkamp, B. I. Halperin, and A. Yacoby, Topological superconductivity in a phase-controlled josephson junction, *Nature* **569**, 93 (2019).
- [31] W. A. Benalcazar, B. A. Bernevig, and T. L. Hughes, Quantized electric multipole insulators, *Science* **357**, 61 (2017).
- [32] W. A. Benalcazar, B. A. Bernevig, and T. L. Hughes, Electric multipole moments, topological multipole moment pumping, and chiral hinge states in crystalline insulators, *Phys. Rev. B* **96**, 245115 (2017).
- [33] Z. Song, Z. Fang, and C. Fang,  $(d - 2)$ -Dimensional Edge States of Rotation Symmetry Protected Topological States, *Phys. Rev. Lett.* **119**, 246402 (2017).

- [34] J. Langbehn, Y. Peng, L. Trifunovic, F. von Oppen, and P. W. Brouwer, Reflection-symmetric second-order topological insulators and superconductors, *Phys. Rev. Lett.* **119**, 246401 (2017).
- [35] F. Schindler, A. M. Cook, M. G. Vergniory, Z. Wang, S. S. P. Parkin, B. A. Bernevig, and T. Neupert, Higher-order topological insulators, *Science Advances* **4**, eaat0346 (2018).
- [36] M. Geier, L. Trifunovic, M. Hoskam, and P. W. Brouwer, Second-order topological insulators and superconductors with an order-two crystalline symmetry, *Phys. Rev. B* **97**, 205135 (2018).
- [37] E. Khalaf, Higher-order topological insulators and superconductors protected by inversion symmetry, *Phys. Rev. B* **97**, 205136 (2018).
- [38] X. Zhu, Tunable Majorana corner states in a two-dimensional second-order topological superconductor induced by magnetic fields, *Phys. Rev. B* **97**, 205134 (2018).
- [39] Z. Yan, F. Song, and Z. Wang, Majorana Corner Modes in a High-Temperature Platform, *Phys. Rev. Lett.* **121**, 096803 (2018).
- [40] Y. Wang, M. Lin, and T. L. Hughes, Weak-pairing higher order topological superconductors, *Phys. Rev. B* **98**, 165144 (2018).
- [41] Q. Wang, C.-C. Liu, Y.-M. Lu, and F. Zhang, High-Temperature Majorana Corner States, *Phys. Rev. Lett.* **121**, 186801 (2018).
- [42] T. Liu, J. J. He, and F. Nori, Majorana corner states in a two-dimensional magnetic topological insulator on a high-temperature superconductor, *Phys. Rev. B* **98**, 245413 (2018).
- [43] C.-H. Hsu, P. Stano, J. Klinovaja, and D. Loss, Majorana Kramers Pairs in Higher-Order Topological Insulators, *Phys. Rev. Lett.* **121**, 196801 (2018).
- [44] Z. Wu, Z. Yan, and W. Huang, Higher-order topological superconductivity: Possible realization in fermi gases and  $\text{Sr}_2\text{RuO}_4$ , *Phys. Rev. B* **99**, 020508 (2019).
- [45] Z. Yan, Higher-order topological odd-parity superconductors, *Phys. Rev. Lett.* **123**, 177001 (2019).
- [46] Z. Yan, Majorana corner and hinge modes in second-order topological insulator/superconductor heterostructures, *Phys. Rev. B* **100**, 205406 (2019).
- [47] Y. Volpez, D. Loss, and J. Klinovaja, Second-order topological superconductivity in  $\pi$ -junction rashba layers, *Phys. Rev. Lett.* **122**, 126402 (2019).
- [48] R.-X. Zhang, W. S. Cole, and S. Das Sarma, Helical hinge majorana modes in iron-based superconductors, *Phys. Rev. Lett.* **122**, 187001 (2019).
- [49] R.-X. Zhang, W. S. Cole, X. Wu, and S. Das Sarma, Higher-order topology and nodal topological superconductivity in  $\text{Fe}(\text{Se},\text{Te})$  heterostructures, *Phys. Rev. Lett.* **123**, 167001 (2019).
- [50] X.-H. Pan, K.-J. Yang, L. Chen, G. Xu, C.-X. Liu, and X. Liu, Lattice-symmetry-assisted second-order topological superconductors and majorana patterns, *Phys. Rev. Lett.* **123**, 156801 (2019).
- [51] X. Zhu, Second-order topological superconductors with mixed pairing, *Phys. Rev. Lett.* **122**, 236401 (2019).
- [52] S. A. A. Ghorashi, X. Hu, T. L. Hughes, and E. Rossi, Second-order dirac superconductors and magnetic field induced majorana hinge modes, *Phys. Rev. B* **100**, 020509 (2019).
- [53] J. Ahn and B.-J. Yang, Higher-order topological superconductivity of spin-polarized fermions, *Phys. Rev. Research* **2**, 012060 (2020).
- [54] Y.-T. Hsu, W. S. Cole, R.-X. Zhang, and J. D. Sau, Inversion-protected higher-order topological superconductivity in monolayer  $\text{wTe}_2$ , *Phys. Rev. Lett.* **125**, 097001 (2020).
- [55] Y.-J. Wu, J. Hou, Y.-M. Li, X.-W. Luo, X. Shi, and C. Zhang, In-plane zeeman-field-induced majorana corner and hinge modes in an  $s$ -wave superconductor heterostructure, *Phys. Rev. Lett.* **124**, 227001 (2020).
- [56] M. Kheirkhah, Z. Yan, Y. Nagai, and F. Marsiglio, First- and second-order topological superconductivity and temperature-driven topological phase transitions in the extended hubbard model with spin-orbit coupling, *Phys. Rev. Lett.* **125**, 017001 (2020).
- [57] S. Franca, D. V. Efremov, and I. C. Fulga, Phase-tunable second-order topological superconductor, *Phys. Rev. B* **100**, 075415 (2019).
- [58] X. Wu, W. A. Benalcazar, Y. Li, R. Thomale, C.-X. Liu, and J. Hu, Boundary-obstructed topological high- $t_c$  superconductivity in iron pnictides, *Phys. Rev. X* **10**, 041014 (2020).
- [59] K. Laubscher, D. Chughtai, D. Loss, and J. Klinovaja, Kramers pairs of majorana corner states in a topological insulator bilayer, *Phys. Rev. B* **102**, 195401 (2020).
- [60] B. Roy, Higher-order topological superconductors in  $\mathcal{P}$ -,  $\mathcal{T}$ -odd quadrupolar dirac materials, *Phys. Rev. B* **101**, 220506 (2020).
- [61] B.-X. Li and Z. Yan, Boundary topological superconductors, *Phys. Rev. B* **103**, 064512 (2021).
- [62] X.-J. Luo, X.-H. Pan, and X. Liu, Higher-order topological superconductors based on weak topological insulators, *Phys. Rev. B* **104**, 104510 (2021).
- [63] A. K. Ghosh, T. Nag, and A. Saha, Hierarchy of higher-order topological superconductors in three dimensions, *Phys. Rev. B* **104**, 134508 (2021).
- [64] S. Qin, C. Fang, F.-C. Zhang, and J. Hu, Topological Superconductivity in an Extended  $s$ -Wave Superconductor and Its Implication to Iron-Based Superconductors, *Phys. Rev. X* **12**, 011030 (2022).
- [65] H. D. Scammell, J. Ingham, M. Geier, and T. Li, Intrinsic first- and higher-order topological superconductivity in a doped topological insulator, *Phys. Rev. B* **105**, 195149 (2022).
- [66] A. Jahin and Y. Wang, Higher-order topological superconductivity in monolayer  $\text{wTe}_2$  from repulsive interactions, *Phys. Rev. B* **108**, 014509 (2023).
- [67] H.-R. Zhang, J.-H. Zhang, Z.-C. Gu, R.-X. Zhang, and S. Yang, Intrinsically interacting higher-order topological superconductors, *Phys. Rev. B* **108**, L060504 (2023).
- [68] Z. Zhang, Z. Wu, C. Fang, F.-c. Zhang, J. Hu, Y. Wang, and S. Qin, Topological superconductivity from unconventional band degeneracy with conventional pairing, *Nature Communications* **15**, 7971 (2024).
- [69] P. Chatterjee, A. K. Ghosh, A. K. Nandy, and A. Saha, Second-order topological superconductor via noncollinear magnetic texture, *Phys. Rev. B* **109**, L041409 (2024).
- [70] P. M. Bonetti, D. Chakraborty, X. Wu, and A. P. Schnyder, Interaction-driven first-order and higher-order topological superconductivity, *Phys. Rev. B* **109**, L180509 (2024).
- [71] S.-B. Zhang, A. Calzona, and B. Trauzettel, All-electrically tunable networks of majorana bound states, *Phys. Rev. B* **102**, 100503 (2020).
- [72] M. F. Lapa, M. Cheng, and Y. Wang, Symmetry-protected gates of Majorana qubits in a high- $T_c$  higher-order topological superconductor platform, *SciPost Phys.* **11**, 86 (2021).
- [73] D. Zhu, B.-X. Li, and Z. Yan, Sublattice-sensitive majorana modes, *Phys. Rev. B* **106**, 245418 (2022).
- [74] M. Kheirkhah, D. Zhu, J. Maciejko, and Z. Yan, Corner- and sublattice-sensitive majorana zero modes on the kagome lattice, *Phys. Rev. B* **106**, 085420 (2022).

- [75] D. Zhu, M. Kheirkhah, and Z. Yan, Sublattice-enriched tunability of bound states in second-order topological insulators and superconductors, *Phys. Rev. B* **107**, 085407 (2023).
- [76] L. Liu, C. Miao, H. Tang, Y.-T. Zhang, and Z. Qiao, Magnetically controlled topological braiding with majorana corner states in second-order topological superconductors, *Phys. Rev. B* **109**, 115413 (2024).
- [77] L. Trifunovic and P. W. Brouwer, Higher-order bulk-boundary correspondence for topological crystalline phases, *Phys. Rev. X* **9**, 011012 (2019).
- [78] A. Haim and Y. Oreg, Time-reversal-invariant topological superconductivity in one and two dimensions, *Physics Reports* **825**, 1 (2019), time-reversal-invariant topological superconductivity in one and two dimensions.
- [79] L. Fu and E. Berg, Odd-parity topological superconductors: Theory and application to  $\text{Cu}_x\text{Bi}_2\text{Se}_3$ , *Phys. Rev. Lett.* **105**, 097001 (2010).
- [80] M. Sato, Topological odd-parity superconductors, *Phys. Rev. B* **81**, 220504 (2010).
- [81] X.-L. Qi, T. L. Hughes, and S.-C. Zhang, Topological invariants for the fermi surface of a time-reversal-invariant superconductor, *Phys. Rev. B* **81**, 134508 (2010).
- [82] J. Wang, Y. Xu, and S.-C. Zhang, Two-dimensional time-reversal-invariant topological superconductivity in a doped quantum spin-Hall insulator, *Phys. Rev. B* **90**, 054503 (2014).
- [83] G.-H. Feng, H.-H. Zhang, and Z. Yan, Time-reversal invariant topological gapped phases in bilayer dirac materials, *Phys. Rev. B* **106**, 064509 (2022).
- [84] S. Deng, L. Viola, and G. Ortiz, Majorana modes in time-reversal invariant  $s$ -wave topological superconductors, *Phys. Rev. Lett.* **108**, 036803 (2012).
- [85] S. Nakosai, Y. Tanaka, and N. Nagaosa, Topological superconductivity in bilayer rashba system, *Phys. Rev. Lett.* **108**, 147003 (2012).
- [86] Q.-S. Xu, Z.-M. Wang, L.-H. Hu, R. Wang, and D.-H. Xu, Helical  $f$ -Wave Superconductivity in Cubic Rashba Superconductors, *arXiv e-prints*, [arXiv:2408.02008](https://arxiv.org/abs/2408.02008) (2024), [arXiv:2408.02008 \[cond-mat.supr-con\]](https://arxiv.org/abs/2408.02008).
- [87] J. M. Midtgaard, Z. Wu, and G. M. Bruun, Time-reversal-invariant topological superfluids in bose-fermi mixtures, *Phys. Rev. A* **96**, 033605 (2017).
- [88] F. Zhang, C. L. Kane, and E. J. Mele, Time-Reversal-Invariant Topological Superconductivity and Majorana Kramers Pairs, *Phys. Rev. Lett.* **111**, 056402 (2013).
- [89] M. S. Scheurer and J. Schmalian, Topological superconductivity and unconventional pairing in oxide interfaces, *Nature Communications* **6**, 6005 (2015).
- [90] Y. Chen and H.-Y. Kee, Helical majorana fermions and flat edge states in the heterostructures of iridates and high- $T_C$  cuprates, *Phys. Rev. B* **97**, 085155 (2018).
- [91] R.-X. Zhang and S. Das Sarma, Intrinsic time-reversal-invariant topological superconductivity in thin films of iron-based superconductors, *Phys. Rev. Lett.* **126**, 137001 (2021).
- [92] M. Kheirkhah, Z.-Y. Zhuang, J. Maciejko, and Z. Yan, Surface Bogoliubov-Dirac cones and helical Majorana hinge modes in superconducting Dirac semimetals, *Phys. Rev. B* **105**, 014509 (2022).
- [93] F. Parhizgar and A. M. Black-Schaffer, Highly tunable time-reversal-invariant topological superconductivity in topological insulator thin films, *Scientific Reports* **7**, 9817 (2017).
- [94] X.-H. Pan, L. Chen, D. E. Liu, F.-C. Zhang, and X. Liu, Majorana zero modes induced by the meissner effect at small magnetic field, *Phys. Rev. Lett.* **132**, 036602 (2024).
- [95] S. M. Young and C. L. Kane, Dirac semimetals in two dimensions, *Phys. Rev. Lett.* **115**, 126803 (2015).
- [96] G. R. Stewart, Superconductivity in iron compounds, *Rev. Mod. Phys.* **83**, 1589 (2011).
- [97] P. J. Hirschfeld, M. M. Korshunov, and I. I. Mazin, Gap symmetry and structure of fe-based superconductors, *Reports on Progress in Physics* **74**, 124508 (2011).
- [98] A. P. Schnyder, S. Ryu, A. Furusaki, and A. W. W. Ludwig, Classification of topological insulators and superconductors in three spatial dimensions, *Phys. Rev. B* **78**, 195125 (2008).
- [99] A. Kitaev, Periodic table for topological insulators and superconductors, *AIP Conference Proceedings* **1134**, 22 (2009).
- [100] S. Ryu, A. P. Schnyder, A. Furusaki, and A. W. Ludwig, Topological insulators and superconductors: tenfold way and dimensional hierarchy, *New Journal of Physics* **12**, 065010 (2010).
- [101] Y. Mo, X.-J. Wang, Z.-Y. Zhuang, and Z. Yan, Coexistence of Chiral Majorana Edge States and Bogoliubov Fermi Surfaces in Two-Dimensional Nonsymmorphic Dirac Semimetal/Superconductor Heterostructures, *arXiv e-prints*, [arXiv:2411.10851](https://arxiv.org/abs/2411.10851) (2024), [arXiv:2411.10851 \[cond-mat.mes-hall\]](https://arxiv.org/abs/2411.10851).
- [102] H. Yao and S. Ryu, Interaction effect on topological classification of superconductors in two dimensions, *Phys. Rev. B* **88**, 064507 (2013).
- [103] C.-K. Chiu, H. Yao, and S. Ryu, Classification of topological insulators and superconductors in the presence of reflection symmetry, *Phys. Rev. B* **88**, 075142 (2013).
- [104] T. Morimoto and A. Furusaki, Topological classification with additional symmetries from clifford algebras, *Phys. Rev. B* **88**, 125129 (2013).
- [105] Y. Ueno, A. Yamakage, Y. Tanaka, and M. Sato, Symmetry-protected majorana fermions in topological crystalline superconductors: Theory and application to  $\text{Sr}_2\text{RuO}_4$ , *Phys. Rev. Lett.* **111**, 087002 (2013).
- [106] J. C. Y. Teo, L. Fu, and C. L. Kane, Surface states and topological invariants in three-dimensional topological insulators: Application to  $\text{Bi}_{1-x}\text{Sb}_x$ , *Phys. Rev. B* **78**, 045426 (2008).
- [107] F. Zhang, C. L. Kane, and E. J. Mele, Topological Mirror Superconductivity, *Phys. Rev. Lett.* **111**, 056403 (2013).
- [108] Z. Yin, H. Li, Z. Yan, and S. Wan, Multifold majorana corner modes arising from multiple pairs of helical edge states, *Phys. Rev. B* **111**, 085421 (2025).
- [109] X. Zhu, Direct demonstration of bulk-boundary correspondence in higher-order topological superconductors with chiral symmetry, *Phys. Rev. B* **110**, 075103 (2024).
- [110] J. Kim, S. S. Baik, S. W. Jung, Y. Sohn, S. H. Ryu, H. J. Choi, B.-J. Yang, and K. S. Kim, Two-dimensional dirac fermions protected by space-time inversion symmetry in black phosphorus, *Phys. Rev. Lett.* **119**, 226801 (2017).
- [111] S. M. Young and B. J. Wieder, Filling-enforced magnetic dirac semimetals in two dimensions, *Phys. Rev. Lett.* **118**, 186401 (2017).
- [112] S. Li, Y. Liu, S.-S. Wang, Z.-M. Yu, S. Guan, X.-L. Sheng, Y. Yao, and S. A. Yang, Nonsymmorphic-symmetry-protected hourglass Dirac loop, nodal line, and Dirac point in bulk and monolayer  $\text{X}_3\text{SiTe}_6$  ( $X = \text{Ta, Nb}$ ), *Phys. Rev. B* **97**, 045131 (2018).
- [113] T. Sato, Z. Wang, K. Nakayama, S. Souma, D. Takane, Y. Nakata, H. Iwasawa, C. Cacho, T. Kim, T. Takahashi, and Y. Ando, Observation of band crossings protected by nonsymmorphic symmetry in the layered ternary telluride  $\text{Ta}_3\text{SiTe}_6$ , *Phys. Rev. B* **98**, 121111 (2018).

- [114] Y. J. Jin, B. B. Zheng, X. L. Xiao, Z. J. Chen, Y. Xu, and H. Xu, Two-dimensional dirac semimetals without inversion symmetry, *Phys. Rev. Lett.* **125**, 116402 (2020).
- [115] L. Chen, L. Zhou, Y. Zhou, C. Liu, Z. Guo, K. Liao, S. Gao, W. Fan, J. Xu, Y. Guo, J. Wang, T. Qian, H. Weng, and G. Wang, Multiple dirac points including potential spin-orbit dirac points in nonsymmorphic  $\text{hfg}_{0.92}\text{te}$ , *Science China Physics, Mechanics & Astronomy* **66**, 217011 (2022).
- [116] W. Meng, Y. Liu, W.-W. Yu, X. Zhang, and G. Liu, Spin-orbital robust dirac points in two-dimensional systems, *Materials Today Physics* **27**, 100774 (2022).